

Article

# Photothermal Killing of A549 Cells and Autophagy Induction by Bismuth Selenide Particles

Yue You <sup>1,†</sup> , Jinxia Li <sup>1,†</sup>, Linlin Chen <sup>1</sup>, Mei Wang <sup>1</sup>, Xinghua Dong <sup>1</sup>, Liang Yan <sup>1</sup>, Aiping Zhang <sup>2</sup> and Feng Zhao <sup>1,\*</sup> 

- <sup>1</sup> CAS Key Laboratory for Biomedical Effects of Nanomaterials and Nanosafety, Institute of High Energy Physics, Chinese Academy of Sciences (CAS), Beijing 100049, China; youyue@ihep.ac.cn (Y.Y.); lijinxia@ihep.ac.cn (J.L.); chenll@ihep.ac.cn (L.C.); wangmei@ihep.ac.cn (M.W.); dongxh@ihep.ac.cn (X.D.); yanliang@ihep.ac.cn (L.Y.)
- <sup>2</sup> Department of Pharmaceutical Analysis, College of Pharmacy, Shanxi Medical University, Taiyuan 030001, China; zhanganp1@163.com
- \* Correspondence: zhaof@ihep.ac.cn
- † These authors contributed equally.

**Abstract:** With a highly efficient optical absorption capability, bismuth selenide (Bi<sub>2</sub>Se<sub>3</sub>) can be used as an outstanding photothermal agent for anti-tumor treatment and shows promise in the field of nanotechnology-based biomedicine. However, little research has been completed on the relevant mechanism underlying the photothermal killing effect of Bi<sub>2</sub>Se<sub>3</sub>. Herein, the photothermal effects of Bi<sub>2</sub>Se<sub>3</sub> particles on A549 cells were explored with emphasis put on autophagy. First, we characterized the structure and physicochemical property of the synthesized Bi<sub>2</sub>Se<sub>3</sub> and confirmed their excellent photothermal conversion efficiency (35.72%), photostability, biocompatibility and ability of photothermal killing on A549 cells. Enhanced autophagy was detected in Bi<sub>2</sub>Se<sub>3</sub>-exposed cells under an 808 nm laser. Consistently, an elevated expression ratio of microtubule-associated protein 1 light chain 3-II (LC3-II) to LC3-I, a marker of autophagy occurrence, was induced in Bi<sub>2</sub>Se<sub>3</sub>-exposed cells upon near infrared (NIR) irradiation. Meanwhile, the expression of cleaved-PARP was increased in the irradiated cells dependently on the exposure concentrations of Bi<sub>2</sub>Se<sub>3</sub> particles. Pharmacological inhibition of autophagy by 3-methyladenine (3-MA) further strengthened the photothermal killing effect of Bi<sub>2</sub>Se<sub>3</sub>. Meanwhile, stress-related signaling pathways, including p38 and stress activated protein kinase/c-Jun N-terminal kinase (SAPK/JNK), were activated, coupled with the attenuated PI3K/Akt signaling. Our study finds that autophagy and the activation of stress-related signaling pathways are involved in the photothermal killing of cancerous cells by Bi<sub>2</sub>Se<sub>3</sub>, which provides a more understanding of photothermal materials.

**Keywords:** bismuth selenide; photothermal killing; apoptosis; autophagy; stress-related signaling pathway



**Citation:** You, Y.; Li, J.; Chen, L.; Wang, M.; Dong, X.; Yan, L.; Zhang, A.; Zhao, F. Photothermal Killing of A549 Cells and Autophagy Induction by Bismuth Selenide Particles. *Materials* **2021**, *14*, 3373. <https://doi.org/10.3390/ma14123373>

Academic Editor: Montserrat Colilla

Received: 9 May 2021

Accepted: 10 June 2021

Published: 18 June 2021

**Publisher's Note:** MDPI stays neutral with regard to jurisdictional claims in published maps and institutional affiliations.



**Copyright:** © 2021 by the authors. Licensee MDPI, Basel, Switzerland. This article is an open access article distributed under the terms and conditions of the Creative Commons Attribution (CC BY) license (<https://creativecommons.org/licenses/by/4.0/>).

## 1. Introduction

Nowadays, the development of strategies to completely cure cancer is still a great challenge. Novel technologies for fighting cancer are expected to be developed with enhanced efficiency, decreased toxicity and reversed drug multi-resistance. In recent years, photothermal therapy (PTT) has been gradually accepted for tumor therapy owing to its excellent effectiveness with minimal invasiveness and good compatibility [1,2]. It has also been used as an adjunct to pre-cancerous lesions and reduced residual tumor burden after operation [3,4]. It also can cooperate with traditional chemotherapy and radiotherapy in improving cancer treatment [5]. Under light irradiation, photothermal agents convert light energy into heat energy and increase the intratumoral temperature, leading to the death of cancer cells [6,7]. Thus, it is feasible to target the lesions directly, non-invasively to the surrounding healthy tissues.

This proves that the efficiency of PTT largely depends on the targeting capability of photothermal agents and their photothermal conversion efficiency [8]. The current research on photothermal therapy is focused on rapidly developing nanomaterials with great PTT potentials arising from the unique physiochemical properties of nanostructures, including a strong optical absorption, an enhanced photothermal conversion efficiency, a controllable surface multi-functionalization and the ability to deeply penetrate tissues [9]. Quite differently from the organic dyes with a lower near-infrared (NIR) light absorption coefficient and severe photobleaching, nanomaterials have shown good performance as photothermal agents in PTT [10]. Many nanomaterials have been reported to have excellent performances as photothermal agents. Among them, metal-containing nanoparticles have attracted great attention for photothermal conversion owing to their excellent photothermal conversion ability and good biocompatibility [11]. In recent years, bismuth-based nanomaterials have been introduced as attractive theranostic agents due to their extraordinary thermoelectric, photoelectric and optical properties [12,13]. Bismuth (Bi) has been used extensively as a medicine for its gastroprotective effects and also has great potential for medical bioimaging owing to its high atomic number [14,15]. Selenium (Se), one of the important trace elements in human, is present as the organ formations of selenocysteine and selenomethionine in the human body. It is essential for many enzymes' activities and has also been reported in immunoregulation and cancer prevention. Bismuth-based nanomaterials, for instance, bismuth selenide, ( $\text{Bi}_2\text{Se}_3$ ), has aroused intense interest among scientists. Importantly,  $\text{Bi}_2\text{Se}_3$  has favorable biocompatibility, greatly facilitating their promising application.  $\text{Bi}_2\text{Se}_3$  was reported to be degraded, and Se released from  $\text{Bi}_2\text{Se}_3$  played an important role through selenoproteins to protect membranes and tissues [16], prevent cancers [17,18] and regulate immunity [19]. It was reported that  $\text{Bi}_2\text{Se}_3$  nanoplates were intraperitoneally injected into mice at a high dose of 20 mg/kg and finally, 93% nanoplates were metabolized with few side-effects within the 90-day long-term period [20]. Based on the good safety profile of  $\text{Bi}_2\text{Se}_3$  nanomaterials, the research on their potential applications has attracted great attention.  $\text{Bi}_2\text{Se}_3$  has been used to develop promising theranostics platforms for cancer therapy by virtue of its good safety profile, excellent X-ray computerized tomographic (CT) imaging and photoacoustic imaging, coupled with photothermal and photodynamic therapeutic effects [21]. The ultra-thin  $\text{Bi}_2\text{Se}_3$  nanoparticles synthesized by Xie et al. were reported to produce a significant tumor photothermal effect with a good photothermal conversion capacity [22]. Macrophage membrane-camouflaged hollow  $\text{Bi}_2\text{Se}_3$  nanoparticles loaded with quercetin were found to increase photothermal sensitivity and potently inhibit lung metastasis of breast cancer [23]. All of these reports have revealed the satisfactory performances of  $\text{Bi}_2\text{Se}_3$  in PTT. However, the molecular mechanism underlying the photothermal effect of  $\text{Bi}_2\text{Se}_3$  nanomaterials remains elusive and needs further exploration.

Autophagy, a self-degradative system, plays a vital role in maintaining cellular homeostasis [24]. It is usually considered as a self-defense mechanism and defends cells from various environmental stimulation and cellular stresses such as heat, hypoxia, DNA damage, reactive oxygen species (ROS) and aggregation of misfolded proteins. Afterward, autophagy was found to be intimately implicated in cancer [25], and targeting autophagy has been regarded as a promising strategy for cancer treatment [26]. However, accumulating evidence has demonstrated that the effect of autophagy on cancer may be sophisticated and depends on tumor type, development stage and tumor microenvironment [27]. Heat stress has been recognized as a trigger for autophagy [28] and even the involvement of autophagy in the PTT effect has also been reported. Zhou and his colleagues found that autophagy inhibition could sensitize the hyperthermia-induced killing of cancer cells [29]. Afterward, they found that beclin-1-induced autophagy up-regulation might destroy the homeostatic functions of autophagy and activate autophagy death pathways, thus improving the efficacy of photothermal killing [30].

Autophagy may affect apoptosis dependently on the type and state of the cell. Autophagy can contribute to pro-survival pathways, while inappropriate autophagy can cause

cell death [31,32]. Autophagy could be regulated by cell stress-related signal pathways, for instance, stress activated protein kinase/c-Jun N-terminal kinase (SAPK/JNK) [33] pathway and p38 MAP kinases (p38) pathway [34]. SAPK/JNK, a mitogen-activated protein kinases (MAPK) subfamily [35], generally induces apoptosis and growth inhibition in response to some stressors, including UV irradiation and oxidative stress [36]. Many data have indicated the associations between JNK signaling and cancer [37]. Actually, JNK has been considered as an attractive target for therapeutic intervention [38]. JNK activation can inhibit tumor formation and has a pro-apoptotic effect [39]. Similarly, p38 pathway is also activated responsively to various stresses and becomes involved in different cell processes, including autophagy [40] and cell death [41].

In this study, we intend to investigate the photothermal conversion capability as well as the photothermal killing effect of the synthesized  $\text{Bi}_2\text{Se}_3$  particles. Emphasis may be put on the exploration of the underlying biological mechanisms, including autophagy and the stress-related signaling pathways (Figure 1a).

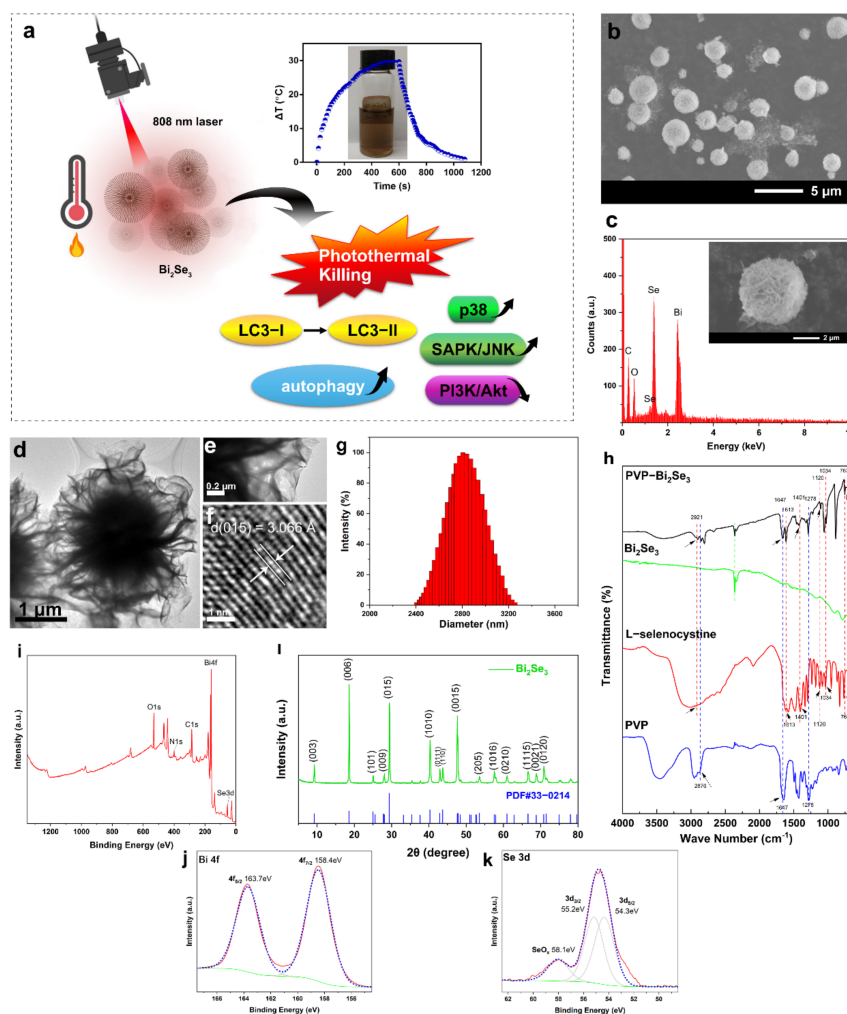


**Figure 1.** Physicochemical characterizations of  $\text{Bi}_2\text{Se}_3$ . (a) Scheme shows that the synthesized  $\text{Bi}_2\text{Se}_3$  performed a remarkable photothermal killing of A549 cells with autophagy involved; (b) SEM image of PVP- $\text{Bi}_2\text{Se}_3$ ; (c) EDS spectrum of  $\text{Bi}_2\text{Se}_3$ . The insert shows a high-magnification SEM image; (d) TEM image of the synthesized  $\text{Bi}_2\text{Se}_3$ ; (e,f) Magnified TEM image; (g) The size distribution of  $\text{Bi}_2\text{Se}_3$  dispersed in water; (h) FTIR spectra of PVP- $\text{Bi}_2\text{Se}_3$ ,  $\text{Bi}_2\text{Se}_3$ , L-selenocysteine and PVP; (i) Survey scan XPS spectrum of PVP- $\text{Bi}_2\text{Se}_3$ ; HR-XPS spectra of (j) Bi 4f and (k) Se 3d scans of PVP- $\text{Bi}_2\text{Se}_3$ . The solid lines represent the data curves, while the dotted lines are the fitted curves; (l) XRD patterns of PVP- $\text{Bi}_2\text{Se}_3$ .

## 2. Materials and Methods

Dimethyl sulfoxide (DMSO), RPMI-1640 culture medium and phosphate buffer solution (PBS) were purchased from Hyclone (Hyclone Laboratories, Logan, UT, USA). Fetal bovine serum (FBS) and penicillin-streptomycin solution were purchased from Gibco (Gibco Invitrogen, Grand Island, NY, USA). Cell-counting kit-8 (CCK-8), Annexin V-FITC/PI assay kit and calcein-AM/PI double stain kit were purchased from Dojindo (Dojindo Laboratories, Tokyo, Japan). All primary antibodies (LC3 $\beta$ , cleaved-PARP, p-p38, p-SAPK/JNK, p-Akt and GAPDH) and secondary antibodies were purchased from Cell Signaling Technology (Cell Signaling Technology, Danvers, MA, USA). ECL prime Western blot detection reagent was purchased from GE Healthcare (GE Healthcare UK Limited, Little Chalfont, Buckinghamshire, UK). All aqueous solutions were prepared from a Milli-Q water system (Merck Millipore, Billerica, MA, USA). A549 human lung adenocarcinoma cell line and human umbilical vein endothelial cells (HUVEC) were obtained from American Type Culture Collection (ATCC).

### 2.1. Characterization of Bi<sub>2</sub>Se<sub>3</sub> Particles

Bi<sub>2</sub>Se<sub>3</sub> particles were synthesized as described in the previous work of our group. In brief, to synthesize Bi<sub>2</sub>Se<sub>3</sub> particles, 1.0 g of poly (vinylpyrrolidone) (PVP) dissolved in 19.5 mL of deionized water was heated to 80 °C in a water bath under argon protection. Then, 10 mL of L-selenocysteine dissolved in deionized water (3 mM) and 0.6 mL of NaOH (0.5 M) were slowly added to the flask and the sample was maintained at 80 °C for 10 min. Afterward, 0.5 mL of Bi (NO<sub>3</sub>)<sub>3</sub> solution (0.1 M) was quickly added to the flask while vigorously stirring. The obtained solution was irradiated with visible light and kept at 80 °C for 3 h. During this period, the color of the solution gradually changed to brownish-black, indicating the formation of the product. As the reaction ended, the mixture was stood to cool to room temperature. The final product was washed three times with deionized water, dialyzed to further remove impurities and finally stored at −20 °C for use. Then, the morphology, size and microstructures of synthesized Bi<sub>2</sub>Se<sub>3</sub> were determined by a field emission scanning electron microscope (SEM, Hitachi S-4800, Tokyo, Japan) and a transmission electron microscope (TEM, Tecnai G2 F20 U-TWIN, Hillsboro, OR, USA). The elemental compositions of the particles were determined with an energy-dispersive spectrometer (EDS) attached to SEM. Dynamic light scattering (DLS) analyzer (NanoBrook Omni) (Brookhaven Instruments, Holtsville, State NY, USA) was used to measure the hydrodynamic diameter and zeta potential of Bi<sub>2</sub>Se<sub>3</sub> dispersion in purified water. Fourier Transform Infrared (FTIR) spectrometer (Thermo Scientific, Waltham, MA, USA) with Nicolet iN10 MX spectrograph (Thermo Scientific, Waltham, MA, USA) was used to record the formation of PVP-Bi<sub>2</sub>Se<sub>3</sub> in the powder form. To detect chemical structures of the formation of Bi<sub>2</sub>Se<sub>3</sub>, X-ray photoelectron spectroscopy (XPS, Thermo Scientific K-alpha, Thermo Scientific, Waltham, MA, USA) measurements were performed to characterize the chemical stoichiometry with monochromatic Al K $\alpha$  radiation (1486.6 eV). X-ray diffraction (XRD) patterns of the sample were performed by a Bruker D8 Advance X-ray diffractometer. The measurements were operated in the reflection mode with Cu K $\alpha$  radiation, and the 2 $\theta$  range between 5° and 80° were recorded.

### 2.2. Photothermal Conversion Performance of Bi<sub>2</sub>Se<sub>3</sub> Particles

UV-visible-near-infrared (UV-Vis-NIR) absorption spectra of Bi<sub>2</sub>Se<sub>3</sub> with different concentrations (100, 200  $\mu$ g/mL) were collected by UV-Vis spectrophotometer (UV 1800, Shimadzu Scientific Instruments, Shimadzu, Japan) with a wavelength coverage of 300–1000 nm. To further detect the photoabsorption capability, the extinction coefficient  $\epsilon$  ( $\lambda$ ) of the Bi<sub>2</sub>Se<sub>3</sub> was calculated. Various concentrations of Bi<sub>2</sub>Se<sub>3</sub> dispersions (0, 25, 50, 100  $\mu$ g/mL) were irradiated with 808 nm laser (VLSM-808-B, CONNET FIBER OPTICS, Shanghai, China) (1.0 W) for 10 min. Calibration and determination of the laser source were performed using a Thorlabs optical power meter (PM100D, THORLABS GmbH, Dachau, Germany) (0.93W), and temperatures were monitored by an infrared thermal

imaging instrument (FLIR i7, FLIR Systems, Wilsonville, OR, USA). The photostability test was performed by irradiating Bi<sub>2</sub>Se<sub>3</sub> dispersion with an 808 nm laser for 10 min and then turning off the laser for four cycles.

### 2.3. CCK-8 Cell Viability Assay

A549 and HUVEC cells were cultivated in RPMI-1640 medium supplemented with 10% fetal bovine serum (FBS), 1% penicillin/streptomycin at 37 °C in a 5% CO<sub>2</sub> and humid atmosphere, respectively. The medium is changed every 2 days until cells are 80% confluence.

To explore the cytotoxicity and photothermal killing effect of Bi<sub>2</sub>Se<sub>3</sub>, A549 and HUVEC cells were seeded into 96-well plates (1 × 10<sup>4</sup> cells/well) and cultured overnight in a 37 °C incubator, respectively. Then, cells were incubated with a fresh medium containing different concentrations of Bi<sub>2</sub>Se<sub>3</sub> (0, 6.25, 12.5, 25, 50, 100, 200 µg/mL) in the absence or presence of laser irradiation. Irradiation was performed using an 808 nm laser with an intensity of 0.21 W/cm<sup>2</sup> and then cells were cultured for a further 12 h. Cell viability was tested using CCK-8 assay. Absorbance was measured in each well at 450 nm using a microplate reader (Victor X3, Perkin Elmer, Waltham, MA, USA).

### 2.4. Live and Dead Assay

Calcein-acetoxymethyl ester (Calcein-AM)/propidium iodide (PI) staining was a routine method for assessing the status of cells based on membrane integrity. Calcein-AM and propidium iodide solutions can stain live and dead cells, respectively. Structurally, the high lipophilicity of methyl acetate helps calcein-AM readily penetrate live cells. AM group can be removed by active esterase in live cells; thus, calcein emits strong green fluorescence. PI can only cross cell membrane that has lost its integrity, where it embeds in DNA double helix and produces red fluorescence. PI stains necrotic or late apoptotic populations, but not early apoptotic cell populations [42].

The well-grown cells were incubated with different concentrations of Bi<sub>2</sub>Se<sub>3</sub> (0, 25, 50, 100, 200 µg/mL) in the absence or presence of laser irradiation. After 10 min of irradiation, cells were further cultured for 12 h and the treatment period ended. For calcein-AM/PI staining, cells were incubated with 2 µM calcein-AM and 2.5 µg/mL PI for 10 min at 37 °C. Representative images were obtained using a fluorescence-inverted microscope system (Olympus IX81, Olympus, Tokyo, Japan).

### 2.5. Annexin V-FITC/PI Double Staining

Annexin V-FITC/PI assay kit was used to evaluate the photothermal killing effect of Bi<sub>2</sub>Se<sub>3</sub>. Well-grown cells were incubated with Bi<sub>2</sub>Se<sub>3</sub> (0, 25, 50 µg/mL) and subject to laser irradiation for 10 min followed by a further incubation of 12 h. Then, all the cells (both the attached and floating cells) were collected by trypsinization and centrifugation. The obtained cells were washed twice using phosphate buffered saline (PBS) solution, resuspended in 500 µL of binding buffer containing 5 µL of annexin V-FITC and 5 µL of PI, then incubated for 15 min in the dark at room temperature. Apoptosis was immediately analyzed by flow cytometry (Accuri C6, USA). After positioning the quadrants on the Annexin V-FITC/PI dot plots, live cells (Annexin V<sup>-</sup>/PI<sup>-</sup>), early apoptotic cells (Annexin<sup>+</sup>/PI<sup>-</sup>), late apoptotic cells (Annexin V<sup>+</sup>/PI<sup>+</sup>) and necrotic cells (Annexin V<sup>-</sup>/PI<sup>+</sup>) were distinguished.

### 2.6. Monodansylcadaverine (MDC) Staining for Autophagy Assay

A549 cells were seeded on confocal dishes (1 × 10<sup>4</sup> cells/mL). After 24 h, cells were incubated with different concentrations of Bi<sub>2</sub>Se<sub>3</sub> dispersions (0, 25, 50 µg/mL) for 6 h in the absence or presence of laser irradiation. At the end of exposure, cells were stained with 50 µM MDC for 20 min and Hoechst 33,342 dye for 5 min in the dark. Then, samples were loaded onto a laser confocal microscope and the representative images were obtained.

## 2.7. Western Blotting Analysis

Western blotting analysis was performed as follows for total proteins. At the end of exposure, A549 cells were washed with ice-cold PBS solution and lysed in RIPA lysis buffer supplemented with complete protease inhibitor cocktails (Roche, Basel, Switzerland) on ice. The solutions of cytolysis were centrifuged (12,000 rpm) for 15 min at 4 °C and the supernatant liquor was collected into cold tubes. The total protein content of each sample was determined using a bicinchoninic acid assay (BCA) protein detection kit (Applygen, Beijing, China). A unit of 20 µg protein was loaded and separated on a 12% sodium dodecyl sulfate-polyacrylamide gel electrophoresis (SDS-PAGE) and transferred onto 0.22 µm polyvinylidene difluoride (PVDF) membrane. Immediately, PVDF membrane was washed three times with Tris-buffered saline Tween-20 (1 × TBST) and then blocked in 5% bovine serum albumin (BSA) for 1 h at room temperature. The membrane was incubated with the indicated primary antibodies, including LC3β (1/3000), cleaved-PARP (1/4000), p-p38 (1/4000), p-SAPK/JNK (1/4000) and p-Akt (1/4000), overnight at 4 °C. PVDF membranes were washed three times with 1 × TBST and incubated with the corresponding peroxidase-conjugated secondary antibodies at room temperature for 1 h followed by three washes. Finally, target proteins were detected after incubation with an electrochemiluminescence (ECL) reagent and immunoreactive bands were captured using a chemiluminescence imaging system (Azure C300, Azure Biosystems, Dublin, CA, USA). GAPDH was used as an internal reference. Band intensity on the exposed film was semi-quantified using ImageJ software (National Institutes of Health, Bethesda, MD, USA). All experiments were repeated at least three times independently.

## 2.8. Statistical Analysis

All experiments in the current study were independently repeated at least 3 times with similar results. The relative percentage and values were presented as the Mean ± Standard Deviation (SD) of six parallel samples. Statistical analysis was performed by two-tailed Student's *t*-test for unpaired data, with  $p < 0.05$  considered statistically significant.

# 3. Results and Discussions

## 3.1. Characterization of Bi<sub>2</sub>Se<sub>3</sub>

Bi<sub>2</sub>Se<sub>3</sub> was synthesized as described in *Methods and Materials*. Figure 1b shows the SEM images of Bi<sub>2</sub>Se<sub>3</sub>. The morphology of the synthesized Bi<sub>2</sub>Se<sub>3</sub> was observed to be flower-like and spherical in shape with a size of ~2.90 µm. Figure 1c shows the corresponding EDS results of the Bi<sub>2</sub>Se<sub>3</sub> sample, confirming the presence of Se and Bi. Typical transmission electron microscopy (TEM) images showed that the synthesized PVP-Bi<sub>2</sub>Se<sub>3</sub> exhibited a relatively uniform structure with an average diameter of ~2.75 µm (Figure 1d). The high-resolution TEM (HRTEM) image presented in Figure 1e,f demonstrated clear lattice fringes with 3.066 Å spacing, corresponding to a lattice spacing of the (015) facets. The results from dynamic light scattering (DLS) analysis revealed that the average hydrated particle size of Bi<sub>2</sub>Se<sub>3</sub> was approximately 2804.13 nm with good dispersion stability (Figure 1g), and their zeta potential was tested to be −32.61 mV. The characteristic peaks of L-selenocysteine included a broad band at 2921 cm<sup>−1</sup> which is assigned to the amino group stretching vibration, and the bands at 1401 and 1613 cm<sup>−1</sup> corresponding to the symmetric and asymmetric flexural vibration of the carboxylic group, respectively (Figure 1h). Besides, the stretching bands of C–N were at 1120 and 1034 cm<sup>−1</sup>, and the stretching band of C–Se was at 767 cm<sup>−1</sup>. The above absorption bands were found in the spectrum of our synthesized Bi<sub>2</sub>Se<sub>3</sub>, revealing the presence of L-selenocysteine on the surface of naked Bi<sub>2</sub>Se<sub>3</sub>. Besides, in the pure PVP spectrum, a very intense peak at 1647 cm<sup>−1</sup> was due to the carbonyl stretching of the five-membered cyclic lactam structure. There were peaks at 2953 and 2876 cm<sup>−1</sup> of spectrum related to C–H stretching for aliphatic compounds [43,44], of which the latter was found in the PVP- Bi<sub>2</sub>Se<sub>3</sub>. The band near 1278 cm<sup>−1</sup> in the pure PVP spectrum due to ring C–N stretching coupled with ring CH<sub>2</sub> wagging [45], which could be observed in the PVP- Bi<sub>2</sub>Se<sub>3</sub> sample FTIR spectrum. This proved that PVP was coated on

the surface of  $\text{Bi}_2\text{Se}_3$ . The typical XPS survey scan spectrum of synthesized  $\text{Bi}_2\text{Se}_3$  shows the presence of Bi, Se and N elements in the sample (Figure 1i). Figure 1j,k shows the high-resolution XPS (HR-XPS) spectra of Bi 4f and Se 3d, respectively. As the Bi 4f spectrum shows (Figure 1j), the binding energies at 158.4 and 163.7 eV are assigned to Bi 4f<sub>7/2</sub> and Bi 4f<sub>5/2</sub>, respectively. The peaks at 54.3 and 55.2 eV are corresponding to Se 3d<sub>5/2</sub> and Se 3d<sub>3/2</sub>, respectively, which are consistent with the reported XPS data of  $\text{Bi}_2\text{Se}_3$  [46–48]. Figure 1k also showed shoulders at 58.1 eV, which resulted from the formation of Se–O bonds, suggesting the oxidation of  $\text{Bi}_2\text{Se}_3$  [47,49], and the oxidation has been reported to be commonly present in  $\text{Bi}_2\text{Se}_3$  [49]. XPS results further confirmed the synthesized  $\text{Bi}_2\text{Se}_3$ , and the Bi and Se atoms of  $\text{Bi}_2\text{Se}_3$  are in the valence state of –2 and +3, respectively. Figure 1l shows XRD patterns of  $\text{Bi}_2\text{Se}_3$  determine a very strong (015) orientation peak, which is consistent with the plane orientation of  $\text{Bi}_2\text{Se}_3$  in the HRTEM result (see Figure 1f). The strong diffraction peaks can be indexed as the layered rhombohedral phase of  $\text{Bi}_2\text{Se}_3$  (JCPDS Card No. 33-0214). The well-defined peaks verified the formation of  $\text{Bi}_2\text{Se}_3$  with high quality.

### 3.2. Photothermal Profile of $\text{Bi}_2\text{Se}_3$

$\text{Bi}_2\text{Se}_3$  powder was dispersed in water and the obtained dispersion was brown-black optically. The UV-visible-NIR absorption spectra of  $\text{Bi}_2\text{Se}_3$  dispersion displayed a certain absorption in the NIR region, suggesting its potential photothermal efficacy (Figure 2a). The molar extinction coefficient  $\epsilon_{808}$  of the  $\text{Bi}_2\text{Se}_3$  was calculated from the measured absorbance in Equation (1) [50,51]:

$$\epsilon_{808} = (A_{808} V \rho N_A) / (LC) \quad (1)$$

where  $A$  is the absorbance of the  $\text{Bi}_2\text{Se}_3$  at 808 nm wavelength (Figure 2a),  $V$  (unit:  $\text{cm}^3$ ) is the average volume of individual  $\text{Bi}_2\text{Se}_3$  and  $\rho$  is the density of the  $\text{Bi}_2\text{Se}_3$  ( $7.51 \text{ g/cm}^3$ ) [52].  $N_A$  is Avogadro's constant,  $L$  is the path length (unit: cm) and  $C$  (unit: g/L) is the weight concentration of the  $\text{Bi}_2\text{Se}_3$  dispersion. The result demonstrated that the  $\text{Bi}_2\text{Se}_3$  particles had a high  $\epsilon$  with  $\sim 1.7 \times 10^{13} \text{ M}^{-1} \cdot \text{cm}^{-1}$  at 808 nm ( $100 \mu\text{g/mL}$ ) (Figure 2b). Besides, to directly evaluate the photothermal conversion capacity of  $\text{Bi}_2\text{Se}_3$  particles, their thermal performance was monitored during laser irradiation of 10 min (Figure 2c). The temperatures of  $\text{Bi}_2\text{Se}_3$  dispersions were tested to increase time- and concentration-dependently under laser irradiation and finally reached a platform, quite differently from the subtle change in the temperature of pure water upon irradiation. The temperature of  $100 \mu\text{g/mL}$   $\text{Bi}_2\text{Se}_3$  dispersion sharply increased to  $56.3 \text{ }^\circ\text{C}$  under laser irradiation (0.93 W), and the temperature increased to  $47.4 \text{ }^\circ\text{C}$  of  $50 \mu\text{g/mL}$   $\text{Bi}_2\text{Se}_3$  dispersion, indicating that the synthesized  $\text{Bi}_2\text{Se}_3$  can efficiently convert 808 nm NIR energy into heat energy. To obtain the heat conversion efficiency ( $\eta$ ) of  $\text{Bi}_2\text{Se}_3$  dispersions ( $100 \mu\text{g/mL}$ ), we recorded the temperature difference ( $\Delta T$ ) under the 808 nm laser. Until the temperature stopped rising, the irradiation source was shut off. The decline of the temperature was monitored (Figure 2d). According to the obtained data, we plotted the linear time data against negative values of the natural logarithm of the driving force temperature obtained from the cooling period (after 600 s) (Figure 2e). The time constant for the heat transfer was calculated to be  $\tau_s = 142.6 \text{ s}$ . Then,  $\eta_{808}$  was calculated by Equation (2) [29,51,53]:

$$\eta_{808} = \frac{hS \Delta T_{max} - Q_s}{I(1 - 10^{-A_{808}})} \quad (2)$$

where  $\Delta T_{max}$  is the maximum stable-state temperature ( $29.67 \text{ }^\circ\text{C}$ ) and  $Q_s$  is the baseline energy input of deionized water, which is determined independently to be  $0.005 \text{ mW}$ .  $I$  is the laser power,  $0.93 \text{ W}$ .  $A_{808}$  is the absorbance at 808 nm (0.15, Figure 2a) and  $hS$  is obtained via Equation (3) [53].

$$hS = \frac{mC}{\tau_s} \quad (3)$$

where  $m$  is the mass (g) of deionized water and  $C$  is heat capacity under constant pressure ( $\text{J/g} \cdot \text{ }^\circ\text{C}$ ). Substituting  $hS$  into Equation (2),  $\eta_{808}$  of  $\text{Bi}_2\text{Se}_3$  can reach  $\sim 31.13\%$ . This result

exhibited a remarkable photothermal conversion capacity possessed by the synthesized  $\text{Bi}_2\text{Se}_3$ . Then, we chose  $50 \mu\text{g/mL}$   $\text{Bi}_2\text{Se}_3$  dispersion for the photostability test. We irradiated  $\text{Bi}_2\text{Se}_3$  dispersion for 10 min for four cycles, separated by 10 min closure of irradiation to allow the temperature recovery, during which the alterations in temperature were carefully monitored. The results demonstrated that the photothermal conversion capacity was still maintained after four continuous heating and cooling cycles of  $\text{Bi}_2\text{Se}_3$  particles, suggesting a good photostability (Figure 2f). Herein, the physicochemical properties of  $\text{Bi}_2\text{Se}_3$  suggested it promising as a prominent photothermal agent.

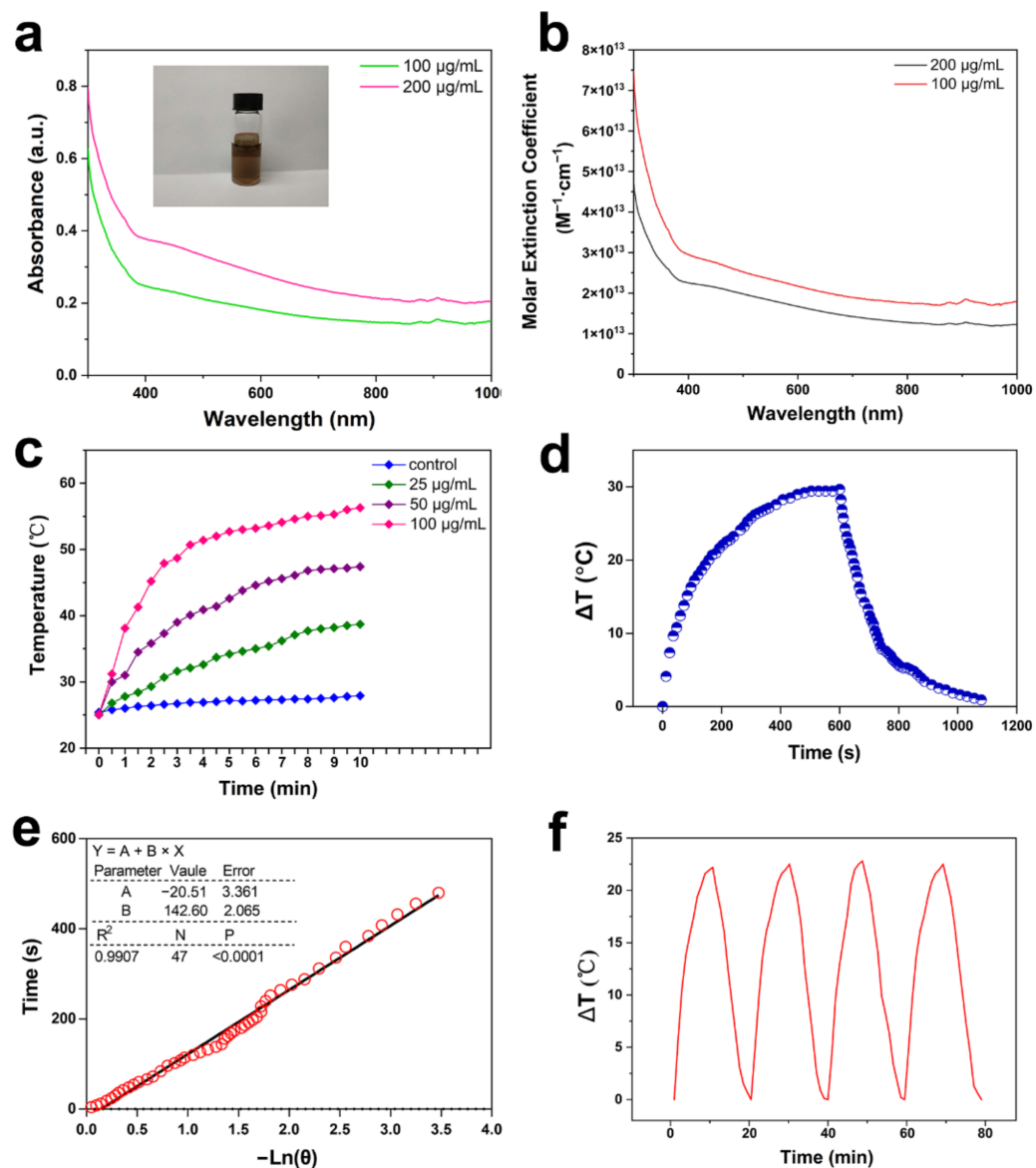


**Figure 2.** Photothermal profile of  $\text{Bi}_2\text{Se}_3$ . (a) Room-temperature UV–Vis–NIR absorbance spectra for the  $\text{Bi}_2\text{Se}_3$  dispersed in deionized water (100, 200  $\mu\text{g/mL}$ ). The Inserted photo shows 100  $\mu\text{g/mL}$   $\text{Bi}_2\text{Se}_3$  dispersion; (b) the extinction coefficient ( $\epsilon$ ) of  $\text{Bi}_2\text{Se}_3$  particles (100, 200  $\mu\text{g/mL}$ ); (c) Temperature elevation curve of  $\text{Bi}_2\text{Se}_3$  dispersion under 808 nm laser ( $0.21 \text{ W/cm}^2$ ); (d) Photothermal effect of  $\text{Bi}_2\text{Se}_3$  dispersion (100  $\mu\text{g/mL}$ ) with laser irradiation (808 nm,  $0.21 \text{ W/cm}^2$ ). The laser was removed after irradiation for 600 s; (e) The calculation of the heat conversion efficiency ( $\eta$ ) of  $\text{Bi}_2\text{Se}_3$  dispersions (100  $\mu\text{g/mL}$ ); (f) Photostability test curve of  $\text{Bi}_2\text{Se}_3$  (50  $\mu\text{g/mL}$ ) within four laser on/off cycles ( $0.21 \text{ W/cm}^2$ ).

### 3.3. The Photothermal Effect of $\text{Bi}_2\text{Se}_3$

It is crucial to assess the cytotoxicity of  $\text{Bi}_2\text{Se}_3$  when considering the potential applications in the biomedical field. Herein, A549 and HUVEC cells were incubated with various concentrations of  $\text{Bi}_2\text{Se}_3$  dispersions ranging from 0 to 200  $\mu\text{g}/\text{mL}$ , and cell viability was tested using a CCK-8 assay (Dojindo Laboratories, Tokyo, Japan) after 24 h. The results demonstrated that  $\text{Bi}_2\text{Se}_3$  was nontoxic to both A549 and HUVEC cells, even at concentrations up to 200  $\mu\text{g}/\text{mL}$  (Figure 3a,b). To investigate the photothermal killing of cancer cells by  $\text{Bi}_2\text{Se}_3$  particles,  $\text{Bi}_2\text{Se}_3$ -incubated A549 cells were irradiated with an 808 nm laser for 10 min and then incubated for a further 12 h without irradiation. The results from the cell viability analysis demonstrated that under laser irradiation,  $\text{Bi}_2\text{Se}_3$  particles induced a concentration-dependent decrease in the viability of A549 cells. Under laser irradiation, the viability of cells incubated with 12.5  $\mu\text{g}/\text{mL}$   $\text{Bi}_2\text{Se}_3$  dispersion was approximately 80% of the control cells, while the cell viability decreased to 25% as the concentration of  $\text{Bi}_2\text{Se}_3$  increased to 200  $\mu\text{g}/\text{mL}$  (Figure 3a). Instead, neither only laser irradiation nor only  $\text{Bi}_2\text{Se}_3$  exposure decreased cell viability. Herein, it showed that both laser irradiation and  $\text{Bi}_2\text{Se}_3$  particles were required for the killing of cancer cells, suggesting a photothermal killing of cancer cells by  $\text{Bi}_2\text{Se}_3$  particles. Meanwhile, the photothermal effect of  $\text{Bi}_2\text{Se}_3$  on HUVEC cells was also tested (Figure 3b). The results revealed that upon laser irradiation, HUVEC cells treated with  $\text{Bi}_2\text{Se}_3$  were damaged at concentrations above 12.5  $\mu\text{g}/\text{mL}$ . Under 808 nm laser irradiation (0.21  $\text{W}/\text{cm}^2$ ), the viability of cells incubated with 12.5  $\mu\text{g}/\text{mL}$   $\text{Bi}_2\text{Se}_3$  dispersion was ~75% of the control cells, while the cell viability decreased to ~13% as the concentration of  $\text{Bi}_2\text{Se}_3$  increased to 200  $\mu\text{g}/\text{mL}$ . This implies that normal cells are probably more sensitive to the photothermal killing of  $\text{Bi}_2\text{Se}_3$  than tumor cells. Considering its potential application, local interventional therapy exploiting PTT effect of  $\text{Bi}_2\text{Se}_3$  is advised to minimize the off-target phototoxicity.

Calcein-AM/PI live–dead staining further confirmed the photothermal killing of  $\text{Bi}_2\text{Se}_3$ . It showed that only green fluorescence existed in the cells incubated with either  $\text{Bi}_2\text{Se}_3$  or irradiation, indicating that no cytotoxicity was induced by only laser irradiation or only  $\text{Bi}_2\text{Se}_3$ . In  $\text{Bi}_2\text{Se}_3$ -exposed cells, upon NIR irradiation, red fluorescence appeared, revealing the photothermal cell death induced by  $\text{Bi}_2\text{Se}_3$ . Moreover, with laser irradiation, more red fluorescent spots were observed in cells incubated with 200  $\mu\text{g}/\text{mL}$   $\text{Bi}_2\text{Se}_3$  dispersion than those incubated with 100  $\mu\text{g}/\text{mL}$  dispersion, exhibiting a concentration-dependent photothermal killing of  $\text{Bi}_2\text{Se}_3$  (Figure 3c). This result was highly consistent with the result from CCK-8 assay, together demonstrating a potent photothermal killing ability of  $\text{Bi}_2\text{Se}_3$  particles advantageous for cancer therapy.

The photothermal killing of A549 cells by  $\text{Bi}_2\text{Se}_3$  was further confirmed using an Annexin V-FITC/PI double-labeling kit (Dojindo Laboratories, Tokyo, Japan). The results from the flow cytometry analysis demonstrated that the apoptosis and necrosis rate of  $\text{Bi}_2\text{Se}_3$ -exposed cells combined with laser irradiation was significantly higher than that of the irradiation-only group or  $\text{Bi}_2\text{Se}_3$ -only exposure group. The death-inducing effect of  $\text{Bi}_2\text{Se}_3$  exposure plus laser irradiation was also shown to be concentration-dependent (Figure 3d). The percentages of healthy, early apoptotic, late apoptotic and necrotic cells in each group were quantified in Figure 3e.

### 3.4. Autophagy Gets Involved in the Photothermal Killing of $\text{Bi}_2\text{Se}_3$

In advance to high-temperature-induced cell death, autophagy is probably triggered to cope with harsh environments and cellular stress [29]. To explore whether autophagy was involved in the photothermal killing effect of  $\text{Bi}_2\text{Se}_3$ , autophagosome formation was observed first using Monodansylcadaverine (MDC) staining (Solarbio, Beijing, China). The results demonstrated that autophagy was induced in  $\text{Bi}_2\text{Se}_3$ -incubated cells upon laser irradiation. The intracellular bright green fluorescence illustrated the formation of autophagosomes in the cytoplasm of A549 cells [54]. slight green fluorescence was present in the control cells with no incubation of  $\text{Bi}_2\text{Se}_3$ . Laser irradiation itself also failed to trigger autophagy, as no obvious green fluorescence was observed in the cytoplasm of

the irradiated cells without  $\text{Bi}_2\text{Se}_3$  incubation. Additionally, no obvious autophagy was induced in  $\text{Bi}_2\text{Se}_3$ -incubated cells with no irradiation. Distinctly, a significant increase in the fluorescence intensity, representing autophagosome formation, was observed in the  $\text{Bi}_2\text{Se}_3$ -incubated cells upon laser irradiation, demonstrating autophagy induction by the photothermal role of  $\text{Bi}_2\text{Se}_3$  (Figure 4a). Furthermore, upon laser irradiation, a higher concentration of  $\text{Bi}_2\text{Se}_3$  exposure triggered more potent autophagy in cells. Then, the green fluorescence intensity in each group of A549 cells was quantified by ImageJ software (Version 1.8.0, 2021, National Institutes of Health, Bethesda, MD, USA) and presented in Figure 4b.

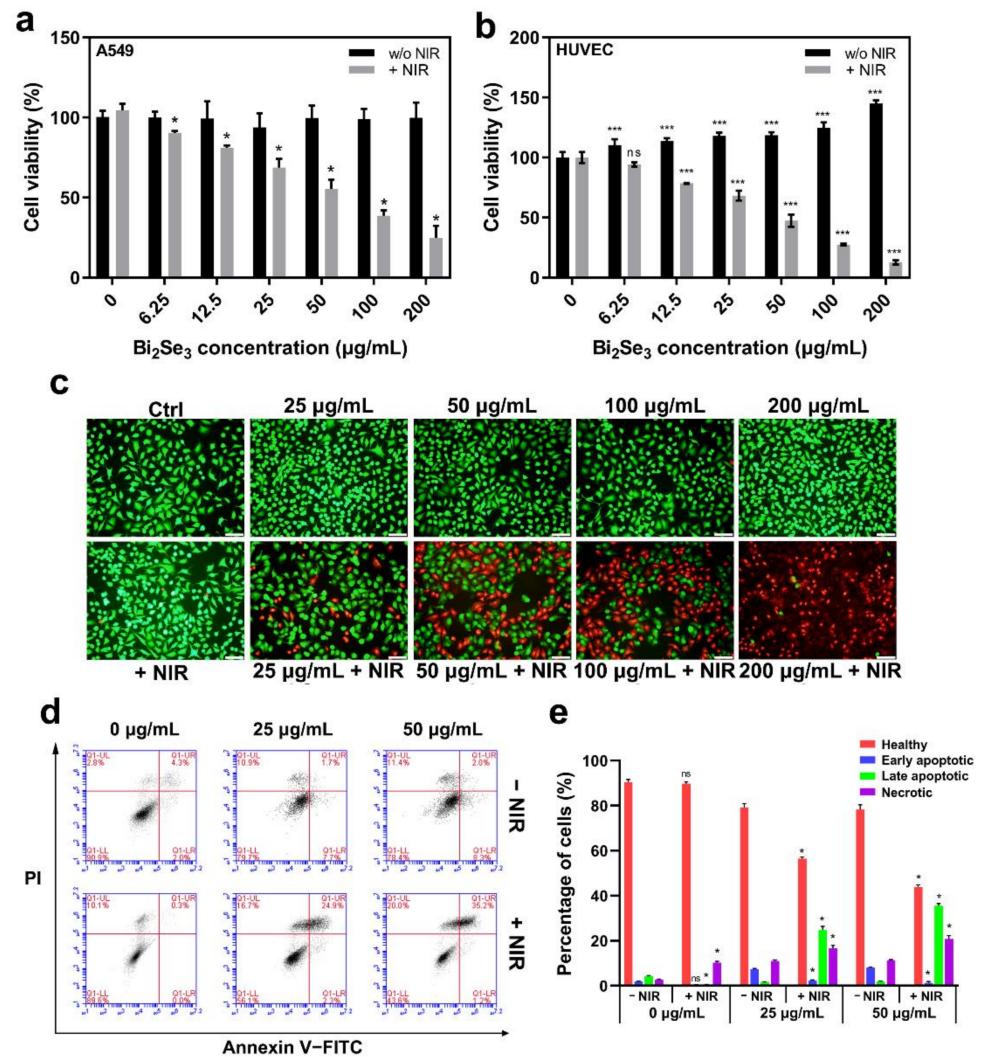


**Figure 3.** Photothermal killing of A549 cells by  $\text{Bi}_2\text{Se}_3$  particles. The viability of A549 cells (a) and HUVEC cells (b) upon  $\text{Bi}_2\text{Se}_3$  exposure (0, 6.25, 12.5, 25, 50, 100, 200  $\mu\text{g/mL}$ ) with or without laser irradiation. \*  $p < 0.05$ , \*\*\*  $p < 0.01$ , versus untreated control group; (c) Live–dead staining of A549 cells. A549 cells were incubated with  $\text{Bi}_2\text{Se}_3$  with or without laser irradiation. Cells with green fluorescence (calcein-positive cells) represent live cells while red fluorescence dead cells (PI-positive cells). Scale bar: 40  $\mu\text{m}$ . The demonstrated images are representative of three independent experiments; (d) Apoptosis analysis by flow cytometry using Annexin V-FITC/PI staining kit. Cells were incubated with  $\text{Bi}_2\text{Se}_3$  (0, 25, 50  $\mu\text{g/mL}$ ) and subjected to laser irradiation for 10 min followed by a further incubation of 12 h. Then, cells were harvested for apoptosis analysis with annexin V-FITC/PI staining. Representative flow cytometry data were presented; (e) The percentages of healthy, early apoptotic, late apoptotic and necrotic apoptotic cells in each group from the results of three independent experiments were quantified (\*  $p < 0.05$ , versus without NIR group).

When autophagy occurs, partial cellular components are encapsulated in autophagosomes and eventually degraded in fusion with lysosomes. Microtubule-associated protein 1 light chain 3 (LC3) is a signature protein of autophagy, composed of cytoplasmic LC3 (LC3-I) and LC3-II spotted on the membrane of autophagosomes [29]. The conversion of LC3 protein from LC3-I to LC3-II is widely recognized as an indicator of autophagy behavior [55]. Autophagy induced by the photothermal effect of  $\text{Bi}_2\text{Se}_3$  was also confirmed by an increased ratio of LC3-II/LC3-I. The results from western blotting analysis demonstrated that the abundance of LC3-II was increased obviously in  $\text{Bi}_2\text{Se}_3$ -exposed cells upon laser irradiation, especially in the group of 50  $\mu\text{g}/\text{mL}$  dispersion (Figure 4c). It should be pointed out that the total expression of LC3 protein (both LC3-I and LC3-II) in the irradiated cells incubated with 100  $\mu\text{g}/\text{mL}$  dispersion displayed a lower level, which was inferred to be related to the accelerated autophagy protein degradation at the high concentration. Compared with other groups, the ratio of LC3-II/I in  $\text{Bi}_2\text{Se}_3$ -exposed cells combined with laser irradiation was significantly higher (Figure 4d), indicating an enhanced autophagy level. Therefore, it confirmed that  $\text{Bi}_2\text{Se}_3$  could induce autophagy in A549 cells under laser irradiation.

Then, we investigated the effect of 3-methyladenine (3-MA), a specific autophagy inhibitor, on the photothermal killing of  $\text{Bi}_2\text{Se}_3$  in vitro. 3-MA, with concentrations of less than 2.5 mM, has marginal effects on the viability of A549 cells (Figure 4e). Notably, 1 h pretreatment of 1 mM 3-MA obviously increased the photothermal killing capability of  $\text{Bi}_2\text{Se}_3$ , as seen from the further decrease in cell viability by 3-MA pretreatment (Figure 4f). The results suggested that autophagy inhibition might enable a more efficient photothermal killing of  $\text{Bi}_2\text{Se}_3$  particles.

To summarize, autophagy was enhanced in A549 cells by  $\text{Bi}_2\text{Se}_3$  particles upon laser irradiation, and autophagy inhibition by 3-MA probably enabled a more efficient photothermal killing of  $\text{Bi}_2\text{Se}_3$ .

### *3.5. Activated Stress-Related p38 and SAPK/JNK Signaling Pathways Coupled with the Attenuated PI3K/Akt Signaling in the Photothermal Effect of $\text{Bi}_2\text{Se}_3$*

As demonstrated above, upon laser irradiation,  $\text{Bi}_2\text{Se}_3$  induced a photothermal killing of cancer cells. In response to the hyperthermal stimuli, the intracellular stress-related signaling pathways, including p38 and p-SAPK/JNK are usually initiated. Using Western blot analysis, the phosphorylation levels of p38 and p-SAPK/JNK were detected to be increased in  $\text{Bi}_2\text{Se}_3$ -incubated cells upon irradiation. Especially in the irradiated cells incubated with 50  $\mu\text{g}/\text{mL}$   $\text{Bi}_2\text{Se}_3$  particles, the phosphorylation levels of p38 and p-SAPK/JNK were dramatically increased, suggesting potent activations of p38 and p-SAPK/JNK signaling pathways. Accordingly, the expression level of cleaved-PARP, an apoptotic marker, was elevated obviously in the cells -incubated with 50  $\mu\text{g}/\text{mL}$   $\text{Bi}_2\text{Se}_3$  upon irradiation (Figure 5a), consistently with the results from CCK-8 and live–dead staining. As expected, PI3K/Akt signaling, which is generally associated with cell survival and growth [56], was significantly attenuated in  $\text{Bi}_2\text{Se}_3$ -exposed cells upon irradiation. The phosphorylation level of Akt in  $\text{Bi}_2\text{Se}_3$ -exposed cells combined with irradiation was significantly reduced (Figure 5a). The results were quantified by ImageJ and demonstrated in Figure 5b with the increased levels of cleaved-PARP, phosphorylated p38 and phosphorylated SAPK/JNK, as well as the decreased level of phosphorylated Akt in  $\text{Bi}_2\text{Se}_3$ -incubated cells upon laser irradiation. Herein, the activated stress-related SAPK/JNK and p38 signaling pathways, coupled with the attenuated PI3K/Akt signaling, were involved in the photothermal killing effect of  $\text{Bi}_2\text{Se}_3$ .

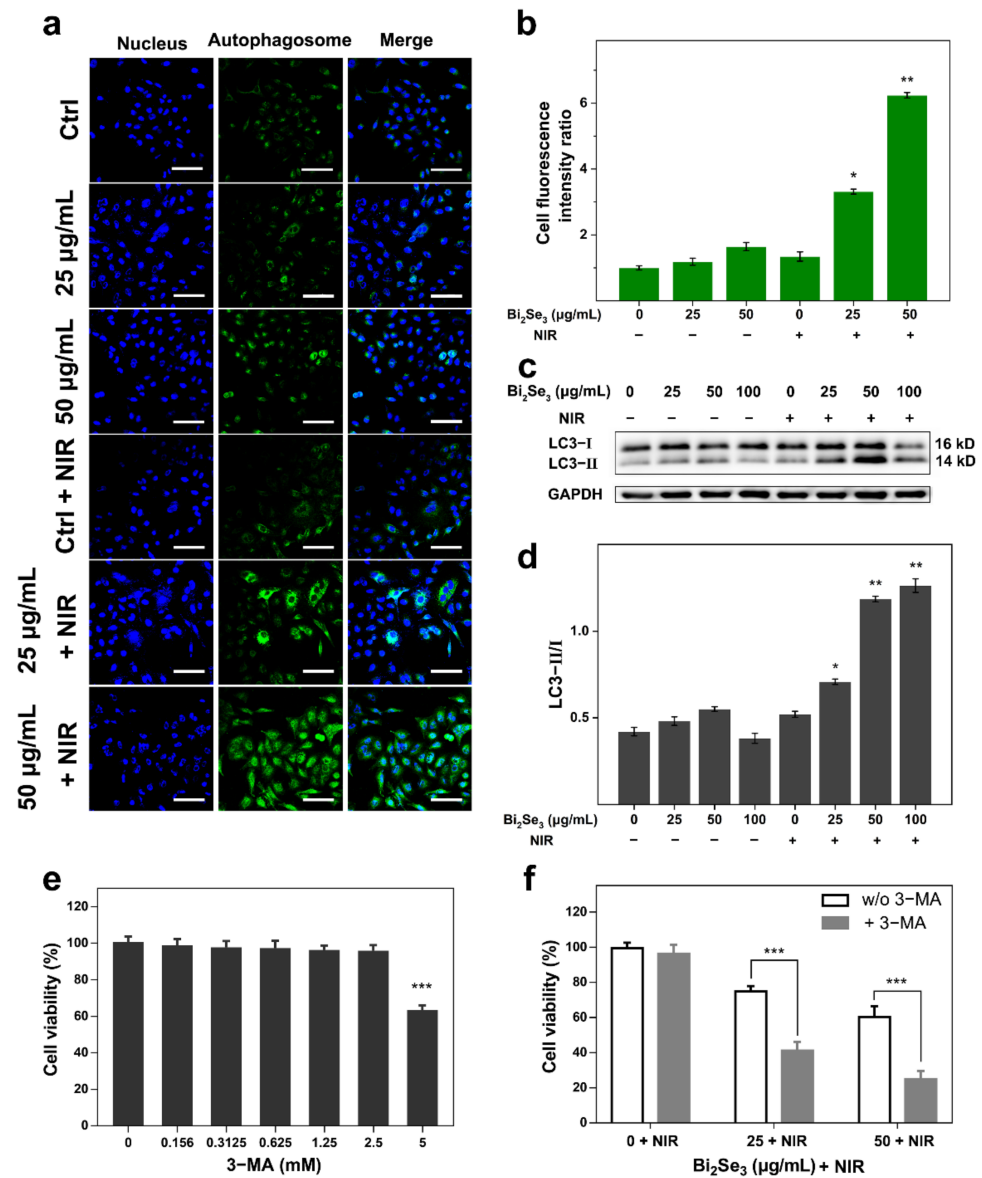


**Figure 4.** Autophagy induced by Bi<sub>2</sub>Se<sub>3</sub> upon laser irradiation. (a) Autophagosome formation in Bi<sub>2</sub>Se<sub>3</sub>-incubated cells upon irradiation as observed by MDC staining. A549 cells were treated with diverse concentrations of Bi<sub>2</sub>Se<sub>3</sub> (0, 25, 50  $\mu\text{g/mL}$ ) with or without laser irradiation. The nucleus was stained with Hoechst 33,342 (Beyotime Institute of Biotechnology, Shanghai, China) (blue) and autophagic vacuole was stained with MDC (green). Representative images were obtained using confocal fluorescence microscopy. Scale bar: 80  $\mu\text{m}$ ; (b) The mean fluorescence intensity of MDC dye in each group of A549 cells of 10 different fields was quantified using ImageJ. \*  $p < 0.05$ , \*\*  $p < 0.01$  versus control group (irradiated cells without Bi<sub>2</sub>Se<sub>3</sub> incubation); (c) The increased LC3 II/I level in Bi<sub>2</sub>Se<sub>3</sub>-exposed cells upon laser irradiation. Cells were exposed to various concentrations of Bi<sub>2</sub>Se<sub>3</sub> (0, 25, 50, 100  $\mu\text{g/mL}$ ) with or without irradiation. GAPDH serves as a loading protein. The representative data of three independent experiments are shown here; (d) The relative expressions of LC3 II/I in each group from the results of three independent experiments were quantified using ImageJ (\*  $p < 0.05$ , \*\*  $p < 0.01$ ); (e) The effect of 3-methyladenine (3-MA) on the basal cell viability of A549 cells; (f) The effect of 3-MA on the photodynamic killing of Bi<sub>2</sub>Se<sub>3</sub>. The data presented are representative of three independent experiments (\*\*\*)  $p < 0.001$ .

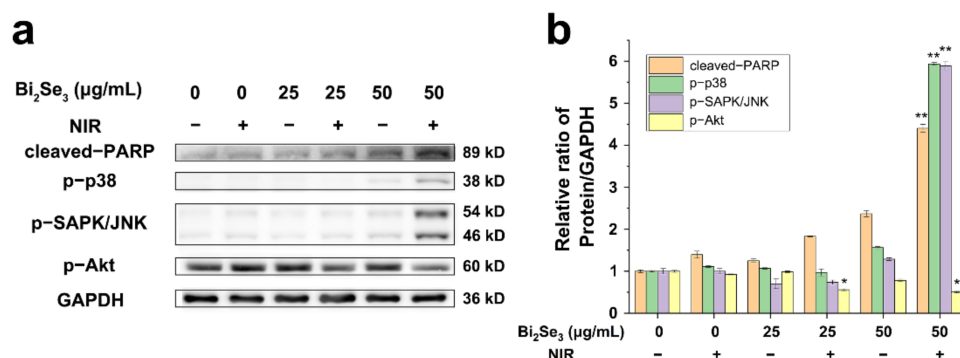


**Figure 5.** Effects of Bi<sub>2</sub>Se<sub>3</sub> on intracellular stress-related and survival-associated signaling pathways. (a) The expressions of cleaved-PARP, phosphorylated p38 (p-p38), phosphorylated SAPK/JNK (p-SAPK/JNK) and phosphorylated Akt (p-Akt) in A549 cells under different conditions by western blot analysis. GAPDH serves as a loading protein. The representative data of three independent experiments are shown here; (b) The bands of these proteins of interest proteins from the results of three independent experiments were quantified using ImageJ. \*  $p < 0.05$ , \*\*  $p < 0.01$  versus control group. The data presented are representative of three independent experiments.

#### 4. Conclusions

In the present work, the synthesized Bi<sub>2</sub>Se<sub>3</sub> exhibited good biocompatibility, excellent photothermal conversion capability and photostability. With laser irradiation, Bi<sub>2</sub>Se<sub>3</sub> performed a significant photothermal killing of A549 cells via apoptosis mechanism. Moreover, autophagy induction was involved in the photothermal effect of Bi<sub>2</sub>Se<sub>3</sub>, which may be a self-protective behavior against the hyperthermal stimuli, as inferred from a more severe cell death triggered by pretreatment of 3-MA. Autophagy inhibition by 3-MA probably enabled a more efficient photothermal therapy. Simultaneously, stress-related p38 and p-SAPK/JNK signaling pathways were obviously activated, accompanied by the attenuated PI3K/Akt signaling. Our work provides new insight into the mechanisms underlying the photothermal effects of Bi<sub>2</sub>Se<sub>3</sub>. The effect of the material-mediated PTT is determined by many external parameters, such as the localization of the materials in the tumor, accumulation of materials within the tumor and interaction between materials and cell-membrane components. The research of these aspects deserves further exploration. Meanwhile, given the potential application, the explorations on the strategy for improving the tumor-targeting performance of Bi<sub>2</sub>Se<sub>3</sub> particles as well as the ADME (absorption, distribution, metabolism and excretion) profile need to be conducted. We also intend to combine the photothermal effect with other therapies to further improve the therapeutic potential of Bi<sub>2</sub>Se<sub>3</sub> for tumor eradication in vivo.

**Author Contributions:** Conceptualization, Y.Y., J.L., X.D. and F.Z.; Formal analysis, L.C.; Funding acquisition, F.Z.; Investigation, Y.Y., L.C. and X.D.; Methodology, Y.Y., J.L., L.C., M.W., X.D., L.Y. and A.Z.; Project administration, F.Z.; Software, Y.Y. and L.C.; Supervision, F.Z.; Visualization, J.L., M.W., L.Y. and A.Z.; Writing—original draft, Y.Y., J.L. and L.C.; Writing—review and editing, Y.Y., J.L. and F.Z. All authors have read and agreed to the published version of the manuscript.

**Funding:** This work was financially supported by NSFC (21301176, 11305182), the Science and Technology Innovation Project of IHEP (Y954513) and National Key Research and Development Program of China (2020YFA0710700).

**Institutional Review Board Statement:** Not applicable.

**Informed Consent Statement:** Not applicable.

**Data Availability Statement:** Data sharing is not applicable to this article.

**Conflicts of Interest:** The authors declare no conflict of interest.

## References

1. Shao, J.; Xie, H.; Huang, H.; Li, Z.; Sun, Z.; Xu, Y.; Xiao, Q.; Yu, X.-F.; Zhao, Y.; Zhang, H.; et al. Biodegradable black phosphorus-based nanospheres for in vivo photothermal cancer therapy. *Nat. Commun.* **2016**, *7*, 12967. [[CrossRef](#)] [[PubMed](#)]
2. Li, X.; Lovell, J.F.; Yoon, J.; Chen, X. Clinical development and potential of photothermal and photodynamic therapies for cancer. *Nat. Rev. Clin. Oncol.* **2020**, *17*, 657–674. [[CrossRef](#)] [[PubMed](#)]
3. Chen, Q.; Xu, L.; Liang, C.; Wang, C.; Peng, R.; Liu, Z. Photothermal therapy with immune-adjuvant nanoparticles together with checkpoint blockade for effective cancer immunotherapy. *Nat. Commun.* **2016**, *7*, 13193. [[CrossRef](#)] [[PubMed](#)]
4. Wang, Y.-T.; Lu, X.-M.; Zhu, F.; Huang, P.; Yu, Y.; Zeng, L.; Long, Z.-Y.; Wu, Y.-M. The use of a gold nanoparticle-based adjuvant to improve the therapeutic efficacy of hNgR-Fc protein immunization in spinal cord-injured rats. *Biomaterials* **2011**, *32*, 7988–7998. [[CrossRef](#)]
5. Li, Z.H.; Chen, Y.J.; Yang, Y.; Yu, Y.; Zhang, Y.H.; Zhu, D.H.; Yu, X.P.; Ouyang, X.X.; Xie, Z.Y.; Zhao, Y.L.; et al. Recent Advances in Nanomaterials-Based Chemo-Photothermal Combination Therapy for Improving Cancer Treatment. *Front. Bioeng. Biotechnol.* **2019**, *7*. [[CrossRef](#)]
6. Shanmugam, V.; Selvakumar, S.; Yeh, C.S. Near-infrared light-responsive nanomaterials in cancer therapeutics. *Chem. Soc. Rev.* **2014**, *43*, 6254–6287. [[CrossRef](#)]
7. Hildebrandt, B.; Wust, P.; Ahlers, O.; Dieing, A.; Sreenivasa, G.; Kerner, T.; Felix, R.; Riess, H. The cellular and molecular basis of hyperthermia. *Crit. Rev. Oncol. Hematol.* **2002**, *43*, 33–56. [[CrossRef](#)]
8. Tan, L.J.; Wu, Z.Y.; Wang, X.J.; Sun, J. Facile synthesis of CuS mesostructures with high photothermal conversion efficiency (vol 5, gp 35317, 2015). *Rsc Adv.* **2015**, *5*, 39192. [[CrossRef](#)]
9. Chen, J.Q.; Ning, C.Y.; Zhou, Z.N.; Yu, P.; Zhu, Y.; Tan, G.X.; Mao, C.B. Nanomaterials as photothermal therapeutic agents. *Prog. Mater. Sci.* **2019**, *99*, 1–26. [[CrossRef](#)]
10. Shibu, E.S.; Hamada, M.; Murase, N.; Biju, V. Nanomaterials formulations for photothermal and photodynamic therapy of cancer. *J. Photochem. Photobiol. C Photochem. Rev.* **2013**, *15*, 53–72. [[CrossRef](#)]
11. Vines, J.B.; Yoon, J.H.; Ryu, N.E.; Lim, D.J.; Park, H. Gold Nanoparticles for Photothermal Cancer Therapy. *Front. Chem.* **2019**, *7*. [[CrossRef](#)]
12. Cheng, X.J.; Yong, Y.; Dai, Y.H.; Song, X.; Yang, G.; Pan, Y.; Ge, C.C. Enhanced Radiotherapy using Bismuth Sulfide Nanoagents Combined with Photo-thermal Treatment. *Theranostics* **2017**, *7*, 4087–4098. [[CrossRef](#)]
13. Wang, L.P.; Long, N.J.; Li, L.H.; Lu, Y.; Li, M.; Cao, J.K.; Zhang, Y.; Zhang, Q.Y.; Xu, S.H.; Yang, Z.M.; et al. Multi-functional bismuth-doped bioglasses: Combining bioactivity and photothermal response for bone tumor treatment and tissue repair. *Light. Sci. Appl.* **2019**, *8*, 54. [[CrossRef](#)]
14. Shahbazi, M.-A.; Faghfour, L.; Ferreira, M.P.A.; Figueiredo, P.; Maleki, H.; Sefat, F.; Hirvonen, J.; Santos, H.A. The versatile biomedical applications of bismuth-based nanoparticles and composites: Therapeutic, diagnostic, biosensing, and regenerative properties. *Chem. Soc. Rev.* **2020**, *49*, 1253–1321. [[CrossRef](#)]
15. Deng, J.; Xu, S.; Hu, W.; Xun, X.; Zheng, L.; Su, M. Tumor targeted, stealthy and degradable bismuth nanoparticles for enhanced X-ray radiation therapy of breast cancer. *Biomaterials* **2018**, *154*, 24–33. [[CrossRef](#)]
16. Rayman, M.P. The importance of selenium to human health. *Lancet* **2000**, *356*, 233–241. [[CrossRef](#)]
17. Rayman, M.P. Selenium in cancer prevention: A review of the evidence and mechanism of action. *Proc. Nutr. Soc.* **2005**, *64*, 527–542. [[CrossRef](#)]
18. Liu, T.; Zeng, L.; Jiang, W.; Fu, Y.; Zheng, W.; Chen, T. Rational design of cancer-targeted selenium nanoparticles to antagonize multidrug resistance in cancer cells. *Nanomed. Nanotechnol. Biol. Med.* **2015**, *11*, 947–958. [[CrossRef](#)]
19. Lee, S.-C.; Lee, N.-H.; Patel, K.D.; Jang, T.-S.; Knowles, J.C.; Kim, H.-W.; Lee, H.-H.; Lee, J.-H. The Effect of Selenium Nanoparticles on the Osteogenic Differentiation of MC3T3-E1 Cells. *Nanomaterials* **2021**, *11*, 557. [[CrossRef](#)]
20. Zhang, X.; Chen, J.; Min, Y.; Park, G.; Shen, X.; Song, S.-S.; Sun, Y.-M.; Wang, H.; Long, W.; Xie, J.; et al. Metabolizable Bi<sub>2</sub>Se<sub>3</sub> Nanoplates: Biodistribution, Toxicity, and Uses for Cancer Radiation Therapy and Imaging. *Adv. Funct. Mater.* **2014**, *24*. [[CrossRef](#)]
21. Li, J.; Jiang, F.; Yang, B.; Song, X.R.; Liu, Y.; Yang, H.H.; Cao, D.R.; Shi, W.R.; Chen, G.N. Topological insulator bismuth selenide as a theranostic platform for simultaneous cancer imaging and therapy. *Sci. Rep.* **2013**, *3*. [[CrossRef](#)]
22. Xie, H.H.; Li, Z.B.; Sun, Z.B.; Shao, J.D.; Yu, X.F.; Guo, Z.N.; Wang, J.H.; Xiao, Q.L.; Wang, H.Y.; Wang, Q.Q.; et al. Metabolizable Ultrathin Bi<sub>2</sub>Se<sub>3</sub> Nanosheets in Imaging-Guided Photothermal Therapy. *Small* **2016**, *12*, 4136–4145. [[CrossRef](#)]
23. Zhao, H.J.; Li, L.; Zhang, J.L.; Zheng, C.X.; Ding, K.L.; Xiao, H.F.; Wang, L.; Zhang, Z.Z. C-C Chemokine Ligand 2 (CCL2) Recruits Macrophage-Membrane-Camouflaged Hollow Bismuth Selenide Nanoparticles To Facilitate Photothermal Sensitivity and Inhibit Lung Metastasis of Breast Cancer. *ACS Appl. Mater. Interfaces* **2018**, *10*, 31124–31135. [[CrossRef](#)]
24. Lee, J.; Giordano, S.; Zhang, J.H. Autophagy, mitochondria and oxidative stress: Cross-talk and redox signalling. *Biochem. J.* **2012**, *441*, 523–540. [[CrossRef](#)]
25. Galluzzi, L.; Pietrocola, F.; Bravo-San Pedro, J.M.; Amaravadi, R.K.; Baehrecke, E.H.; Cecconi, F.; Codogno, P.; Debnath, J.; Gewirtz, D.A.; Karantza, V.; et al. Autophagy in malignant transformation and cancer progression. *Embo J.* **2015**, *34*, 856–880. [[CrossRef](#)]
26. Galluzzi, L.; Bravo-San Pedro, J.M.; Levine, B.; Green, D.R.; Kroemer, G. Pharmacological modulation of autophagy: Therapeutic potential and persisting obstacles. *Nat. Rev. Drug Discov.* **2017**, *16*, 487–511. [[CrossRef](#)]
27. Levy, J.M.M.; Towers, C.G.; Thorburn, A. Targeting autophagy in cancer. *Nat. Rev. Cancer* **2017**, *17*, 528–542. [[CrossRef](#)] [[PubMed](#)]

28. Hale, B.J.; Hager, C.L.; Seibert, J.T.; Selsby, J.T.; Baumgard, L.H.; Keating, A.F.; Ross, J.W. Heat stress induces autophagy in pig ovaries during follicular development. *Biol. Reprod.* **2017**, *97*, 426–437. [[CrossRef](#)] [[PubMed](#)]
29. Zhou, Z.J.; Yan, Y.; Hu, K.W.; Zou, Y.; Li, Y.W.; Ma, R.; Zhang, Q.; Cheng, Y.Y. Autophagy inhibition enabled efficient photothermal therapy at a mild temperature. *Biomaterials* **2017**, *141*, 116–124. [[CrossRef](#)] [[PubMed](#)]
30. Zhou, Z.J.; Yan, Y.; Wang, L.; Zhang, Q.; Cheng, Y.Y. Melanin-like nanoparticles decorated with an autophagy-inducing peptide for efficient targeted photothermal therapy. *Biomaterials* **2019**, *203*, 63–72. [[CrossRef](#)]
31. D'Arcy, M.S. Cell death: A review of the major forms of apoptosis, necrosis and autophagy. *Cell Biol. Int.* **2019**, *43*, 582–592. [[CrossRef](#)]
32. Maiuri, M.C.; Zalckvar, E.; Kimchi, A.; Kroemer, G. Self-eating and self-killing: Crosstalk between autophagy and apoptosis. *Nat. Rev. Mol. Cell Biol.* **2007**, *8*, 741–752. [[CrossRef](#)]
33. Zhou, Y.Y.; Li, Y.; Jiang, W.Q.; Zhou, L.F. MAPK/JNK signalling: A potential autophagy regulation pathway. *Biosci. Rep.* **2015**, *35*. [[CrossRef](#)]
34. Zhong, W.; Zhu, H.; Sheng, F.; Tian, Y.; Zhou, J.; Chen, Y.; Li, S.; Lin, J. Activation of the MAPK11/12/13/14 (p38 MAPK) pathway regulates the transcription of autophagy genes in response to oxidative stress induced by a novel copper complex in HeLa cells. *Autophagy* **2014**, *10*, 1285–1300. [[CrossRef](#)]
35. Braicu, C.; Buse, M.; Busuioc, C.; Drula, R.; Gulei, D.; Raduly, L.; Rusu, A.; Irimie, A.; Atanasov, A.G.; Slaby, O.; et al. A Comprehensive Review on MAPK: A Promising Therapeutic Target in Cancer. *Cancers* **2019**, *11*, 1618. [[CrossRef](#)]
36. Hamdi, M.; Kool, J.; Cornelissen-Steijger, P.; Carlotti, F.; Popeijus, H.E.; van der Burgt, C.; Janssen, J.M.; Yasui, A.; Hoeben, R.C.; Terleth, C.; et al. DNA damage in transcribed genes induces apoptosis via the JNK pathway and the JNK-phosphatase MKP-1. *Oncogene* **2005**, *24*, 7135–7144. [[CrossRef](#)]
37. Hammouda, M.B.; Ford, A.E.; Liu, Y.; Zhang, J.Y. The JNK Signaling Pathway in Inflammatory Skin Disorders and Cancer. *Cells* **2020**, *9*, 857. [[CrossRef](#)]
38. Bubici, C.; Papa, S. JNK signalling in cancer: In need of new, smarter therapeutic targets. *Br. J. Pharmacol.* **2014**, *171*, 24–37. [[CrossRef](#)]
39. Saeki, K.; Kobayashi, N.; Inazawa, Y.; Zhang, H.; Nishitoh, H.; Ichijo, H.; Saeki, K.; Isemura, M.; Yuo, A. Oxidation-triggered c-Jun N-terminal kinase (JNK) and p38 mitogen-activated protein (MAP) kinase pathways for apoptosis in human leukaemic cells stimulated by epigallocatechin-3-gallate (EGCG): A distinct pathway from those of chemically induced and recep. *Biochem. J.* **2002**, *368*, 705–720. [[CrossRef](#)]
40. Sui, X.; Kong, N.; Ye, L.; Han, W.; Zhou, J.; Zhang, Q.; He, C.; Pan, H. p38 and JNK MAPK pathways control the balance of apoptosis and autophagy in response to chemotherapeutic agents. *Cancer Lett.* **2014**, *344*, 174–179. [[CrossRef](#)]
41. Varghese, J.; Chattopadhyaya, S.; Sarin, A. Inhibition of p38 kinase reveals a TNF-alpha-mediated, caspase-dependent, apoptotic death pathway in a human myelomonocyte cell line. *J. Immunol.* **2001**, *166*, 6570–6577. [[CrossRef](#)]
42. Basmaciyani, L.; Azas, N.; Casanova, M. Calcein+/PI- as an early apoptotic feature in Leishmania. *PLoS ONE* **2017**, *12*, e0187756. [[CrossRef](#)]
43. Loría-Bastarrachea, M.I.; Herrera-Kao, W.; Cauich-Rodríguez, J.V.; Cervantes-Uc, J.M.; Vázquez-Torres, H.; Ávila-Ortega, A. A TG/FTIR study on the thermal degradation of poly(vinyl pyrrolidone). *J. Therm. Anal. Calorim.* **2011**, *104*, 737–742. [[CrossRef](#)]
44. Borodko, Y.; Habas, S.E.; Koebel, M.; Yang, P.; Frei, H.; Somorjai, G.A. Probing the interaction of poly(vinylpyrrolidone) with platinum nanocrystals by  $\text{UV}$ - $\text{Raman}$  and  $\text{FTIR}$ . *J. Phys. Chem. B* **2006**, *110*, 23052–23059. [[CrossRef](#)]
45. Zhu, X.; Lu, P.; Chen, W.; Dong, J. Studies of UV crosslinked poly(N-vinylpyrrolidone) hydrogels by FTIR, Raman and solid-state NMR spectroscopies. *Polymer* **2010**, *51*, 3054–3063. [[CrossRef](#)]
46. Han, G.; Chen, Z.-G.; Yang, L.; Wang, L.; Drennan, J.; Zou, J. In-Doped Bi<sub>2</sub>Se<sub>3</sub> Hierarchical Nanostructures as Anode Materials for Li-Ion Batteries. *J. Mater. Chem. A* **2014**, *2*, 7109–7116. [[CrossRef](#)]
47. Du, J.; Gu, Z.; Yan, L.; Yong, Y.; Yi, X.; Zhang, X.; Liu, J.; Wu, R.; Ge, C.; Chen, C.; et al. Poly(Vinylpyrrolidone)- and Selenocysteine-Modified Bi<sub>2</sub>Se<sub>3</sub> Nanoparticles Enhance Radiotherapy Efficacy in Tumors and Promote Radioprotection in Normal Tissues. *Adv. Mater.* **2017**, *29*. [[CrossRef](#)]
48. Kong, D.; Randel, J.C.; Peng, H.; Cha, J.J.; Meister, S.; Lai, K.; Chen, Y.; Shen, Z.-X.; Manoharan, H.C.; Cui, Y. Topological Insulator Nanowires and Nanoribbons. *Nano Lett.* **2010**, *10*, 329–333. [[CrossRef](#)]
49. Kong, D.; Cha, J.; Lai, K.; Peng, H.; Analytis, J.; Meister, S.; Chen, Y.; Zhang, H.-J.; Fisher, I.; Shen, Z.-X.; et al. Rapid Surface Oxidation as a Source of Surface Degradation Factor for Bi<sub>2</sub>Se<sub>3</sub>. *ACS Nano* **2011**, *5*, 4698–4703. [[CrossRef](#)]
50. Zhao, Y.; Pan, H.; Lou, Y.; Qiu, X.; Zhu, J.; Burda, C. Plasmonic Cu<sub>2-x</sub>S Nanocrystals: Optical and Structural Properties of Copper-Deficient Copper(I) Sulfides. *J. Am. Chem. Soc.* **2009**, *131*, 4253–4261. [[CrossRef](#)]
51. Tian, Q.; Jiang, F.; Zou, R.; Liu, Q.; Chen, Z.; Zhu, M.; Yang, S.; Wang, J.; Wang, J.; Hu, J. Hydrophilic Cu<sub>9</sub>S<sub>5</sub> Nanocrystals: A Photothermal Agent with a 25.7% Heat Conversion Efficiency for Photothermal Ablation of Cancer Cells in Vivo. *ACS Nano* **2011**, *5*, 9761–9771. [[CrossRef](#)] [[PubMed](#)]
52. Wells, A.F. *Structural Inorganic Chemistry*, 5th ed.; Clarendon Press: Oxford, UK, 1990.
53. Yin, W.; Yan, L.; Yu, J.; Tian, G.; Zhou, L.; Zheng, X.; Zhang, X.; Yong, Y.; Li, J.; Gu, Z.; et al. High-Throughput Synthesis of Single-Layer MoS<sub>2</sub> Nanosheets as a Near-Infrared Photothermal-Triggered Drug Delivery for Effective Cancer Therapy. *ACS Nano* **2014**, *8*, 6922–6933. [[CrossRef](#)] [[PubMed](#)]

54. Vazquez, C.L.; Colombo, M.I. Assays to assess autophagy induction and fusion of autophagic vacuoles with a degradative compartment, using monodansylcadaverine (MDC) and DQ-BSA. *Methods Enzymol.* **2009**, *452*, 85–95. [[CrossRef](#)] [[PubMed](#)]
55. Gomes-da-Silva, L.C.; Jimenez, A.J.; Sauvat, A.; Xie, W.; Souquere, S.; Divoux, S.; Storch, M.; Sveinbjornsson, B.; Rekdal, O.; Arnaut, L.G.; et al. Recruitment of LC3 to damaged Golgi apparatus. *Cell Death Differ.* **2019**, *26*, 1467–1484. [[CrossRef](#)]
56. Yang, J.; Nie, J.; Ma, X.L.; Wei, Y.Q.; Peng, Y.; Wei, X.W. Targeting PI3K in cancer: Mechanisms and advances in clinical trials. *Mol. Cancer* **2019**, *18*. [[CrossRef](#)]